Photoacoustic probe using a microring resonator ultrasonic sensor for endoscopic applications

Biqin Dong,[1,2] Siyu Chen,[1] Zhen Zhang,[2] Cheng Sun,[2] and Hao F. Zhang[1,*]

[1]*Department of Biomedical Engineering, Northwestern University, Evanston, Illinois 60208, USA*

[2]*Department of Mechanical Engineering, Northwestern University, Evanston, Illinois 60208, USA*

**Corresponding author: hfzhang@northwestern.edu*

Received April 2, 2014; revised May 26, 2014; accepted June 22, 2014;
posted June 24, 2014 (Doc. ID 209396); published July 21, 2014

We designed an all-optical photoacoustic (PA) probe for endoscopic applications by employing an optically transparent, coverslip-type, polymeric microring resonator ultrasonic sensor. We experimentally quantified the axial, tangential, and radial resolutions and angular sensitive stability of this probe. Using this probe, we achieved volumetric imaging of several phantoms. Our all-optical probe design offers clear benefit in integrating PA endoscope with other optical endoscopic imaging modalities to facilitate the transformation from bench to bedside.

OCIS codes: (170.5120) Photoacoustic imaging; (170.2150) Endoscopic imaging; (130.6010) Sensors.
http://dx.doi.org/10.1364/OL.39.004372

Photoacoustic (PA) endoscopy is an attractive novel endoscopic modality due to its capability of realizing photoacoustic microscopy (PAM) in hollow organs with no or minimal invasion. As an emerging label-free imaging technology, PAM offers unprecedented sensitivity to optical absorption contrast with physiologically relevant information [1,2], e.g., oxygen metabolism [3–5] and tumor progression [6], at diffraction-limited spatial resolution. Current PA endoscopic probes mainly use conventional piezoelectric transducers [7–12], which pose several constraints. First, the opaque nature of piezoelectric transducers requires several compromises in the delicate optical design of endoscopic systems, usually resulting in sacrificed spatial resolution and bulky dimension. Second, the sensitivity and detecting frequency bandwidth of piezoelectric transducers can be restricted due to miniaturization [13], leading to reduced signal-to-noise ratio (SNR) and radial resolution. Although transparent indium tin oxide-based piezoelectric transducers have been developed to overcome above limits [14,15], their bandwidth are highly limited and not sufficient for high-resolution PA imaging.

In contrast, optical ultrasound detection methods offer desirable solutions for aforementioned constraints in endoscopic applications. Several integrated photonics based prototypes, such as an intrinsic optical fiber interferometer [16], a waveguide Mach–Zehnder interferometer [17], and Fabry–Perot cavities [18], were introduced to PA endoscopy. Recently, we developed an all-optical PA endoscopic probe using an optically transparent microring resonator (MRR) ultrasonic sensor for PAM [19] that exhibits unique advantages for endoscopic applications. First, the optically transparent fiber-based MRR introduces minimal interference to the existing optical system. Second, highly sensitive ultrasound detection can be achieved by modulations in the effective optical path length and magnified by more than a thousandfold through optical resonance. Third, MRR offers a significantly broader ultrasonic detection bandwidth that, subsequently, improves radial resolution in volumetric imaging and saturation limit in functional PA imaging [17,20].

In this Letter, we demonstrate the feasibility of integrating an MRR ultrasonic sensor into a compact probe for 3D PA endoscopy. The axial, tangential, and radial resolutions of our PA probe can reach 16.0, 15.7, and 4.5 μm, respectively. The sensitivity stability during an angular scan was also characterized experimentally, indicating a good stability over at least 180 deg. Finally, 3D volumetric imaging of several custom phantoms was performed to demonstrate the probe's potential PA imaging abilities in tissue.

Figure 1 shows the design and working principle of the PA endoscopic probe. Figure 1(a) is a photograph of a fully packaged probe, and Fig. 1(b) is the schematic of

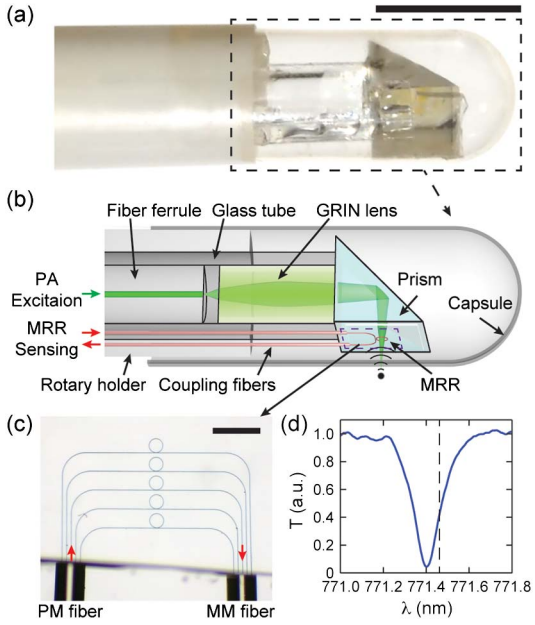

Fig. 1. (a) Photograph of the MRR-based PA endoscopic probe. The outer diameter is 4.5 mm. Bar: 5 mm. (b) Illustration of the probe within the dashed-square in panel (a). (c) Photograph of the packaged MRRs. Bar: 200 μm. (d) Typical transmission spectrum of MRR. T, normalized transmission; λ, wavelength. The dashed-line indicates the operation wavelength of the MRR at 771.46 nm, where $dT/d\lambda$ is maximum.

the probe's design. We used a gradient index (GRIN) lens to focus the PA illuminating light coming out of a single-mode optical fiber (numerical aperture: 0.22). A prism was attached to the end of the GRIN lens for side-view illumination. Then, we glued an MRR ultrasonic sensor onto the side of the prism using UV-curable resin and carefully aligned the MRR to be concentric with the optical illuminating beam.

Details of the MRR ultrasonic sensor are shown in Fig. 1(c). Polymeric MRRs with U-shaped bus waveguides were fabricated on a 250-μm-thick fused quartz microscope coverslip using E-beam lithography and carefully diced to 2 mm × 2 mm. The optical waveguide made from SU-8 has a square-shaped cross-section with a side length of 800 nm [18]. Both the input and output ends of the bus waveguide were precisely cleaved for fiber coupling. A single-mode polarization maintaining (PM) fiber was used to couple a transverse magnetic mode wave from a narrow-band tunable laser (765–780 nm, TLB-6712, New Focus) into the bus waveguide, and a multimode fiber was used to collect the transmitted light from the other end of the waveguide. The guided light wave inside the bus waveguide was evanescently coupled into the ring waveguide across a low-dielectric gap between the bus and ring waveguides. Light circulating inside the ring waveguide led to a strong optical resonance that can be characterized by a narrow dip in the transmission spectrum due to destructive interference [Fig. 1(d)] between lights in the two waveguides. Assuming λ_r is the resonance wavelength, zero transmission at λ_r can be achieved when the intrinsic loss of the ring resonator matches the coupling loss, which is usually referred to as the critical coupling condition. The Q-factor of an MRR can be calculated by $\lambda_r/\Delta\lambda$, where $\Delta\lambda$ is the full width half-maximum of the resonance dip. We fabricated five MRRs with various gap sizes with the arrangement shown in Fig. 1(c) and the one with critical coupling was experimentally selected to be used in the probe. The measured transmission spectrum [Fig. 1(d)] indicates a Q-factor of 4820. The optimal detection sensitivity at the maximum $dT/d\lambda$ is 10.5 at 771.46 nm, which was selected as the MRR operating wavelength.

We constructed a mechanical scanning endoscopic imaging system to characterize the performances of our PA probe and to demonstrate its volumetric PA imaging ability. As shown in Fig. 2, a short-pulse laser (SPOT, Elforlight Ltd.; wavelength: 532 nm, pulse duration: 1 ns) was coupled into a single-mode fiber and focused onto the specimen through the endoscopic probe. The absorbed laser energy led to a transient thermo-elastic expansion

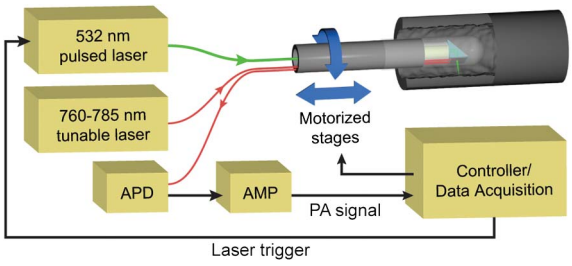

Fig. 2. Schematic of the MRR-based PA endoscopic imaging system. APD, avalanche photodiode; AMP, amplifier.

of the sample and subsequently launched ultrasonic waves with a wide-range of frequency components. The ultrasound pressure induced changes in both the dimension and the refractive index of the polymer waveguide. These changes collectively altered the optical path length of the ring resonator and, thus, caused a shift in the resonant frequency. The shift in resonant frequency was measured as the voltage modulation in the transmitted optical signal by a photodetector. We used a low noise, high-sensitivity photodetector (APD210, Menlo System; bandwidth: 5 MHz – 1 GHz) to record the transmitted light through the bus waveguide. The detected signals were further amplified by 12 dB (FL500NL+, Mini-circurts; bandwidth: 10 MHz – 500 MHz) and digitized by a high-speed digitizer (CobraMax, GaGe; sampling rate: 3 GS/s, bandwidth: 1.5 GHz). Each time-resolved PA signal was then converted to a depth-resolved A-line after Hilbert transformation. The A-lines collected by a circular scan were further converted from the polar coordinate to the Cartesian coordinates by using the trigonometric functions, in order to reconstruct the actual geometry of sample being examined.

Based on the experimental setup aforementioned, the MRR ultrasonic sensor offers a sensitivity of 1.1 V/MPa [19]. The noise level directly measured from the time resolve signal is 0.32 mV, which corresponds to a noise equivalent pressure (NEP) of 352 Pa. The NEP of the MRR ultrasonic sensor is several orders of magnitude better than conventional piezoelectric transducers of comparable size, and it is comparable with the best optical detectors been reported.

The endoscopic probe was mounted on a homemade shaft, which was driven by a step motor for circumferential sector scan (B-scan) at a step size of 0.1125 deg. A second linear motorized stage was used to translate the probe at a step size of 0.625 μm along the axial direction that completed a 2D tangential-axial scan for volumetric imaging. Figure 3 shows the experimentally quantified spatial resolutions of the endoscopic probe. The axial edge spread function (ESF) was recorded by linearly scanning the edge of a piece of black tape [Fig. 3(a)] and the corresponding line spread function (LSF) was calculated by taking the first derivative of the ESF [Fig. 3(b)], suggesting that the axial resolution is 16.0 μm. The tangential ESF is shown in Fig. 3(c) and its corresponding LSF is shown in Fig. 3(d), indicating a tangential resolution of 0.4 deg that can be converted to 15.7 μm when the radius of the imaging scan is 2.25 mm. The detected time-resolved PA impulse response shown in Fig. 3(e) indicates a bandwidth over 250 MHz after performing Fourier transform of the time domain signal. The radial resolution can be estimated by numerically shifting and summing two impulse responses and then evaluating the envelope provided by the Hilbert transformation [21]. As shown in Fig. 3(f), the contrast-to-noise ratio (CNR) was plotted against the shift distance between the two impulse responses and the contrast was defined as the difference between the peaks and the valley in the PA envelope. If we consider that the two peaks can be differentiated when the CNR of the envelope reaches 6 dB, our MRR-based endoscope can easily attain a sub-10-μm axial resolution (up to 4.5 μm). Although the axial, tangential, and radial

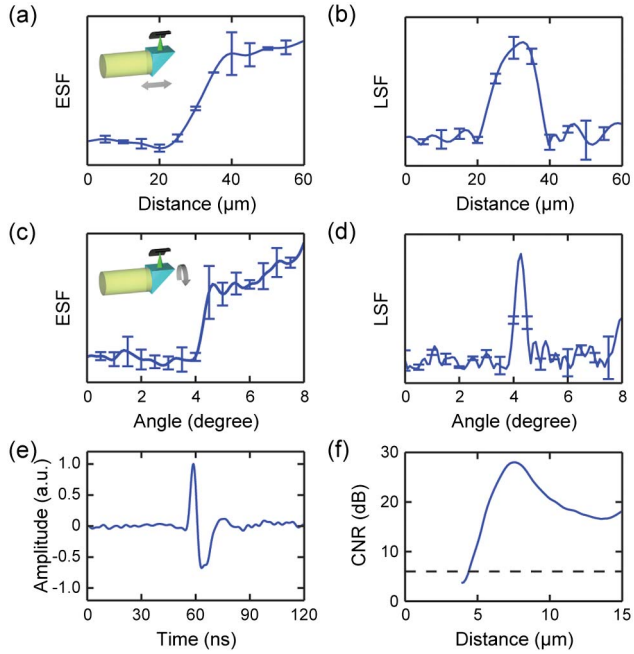

Fig. 3. Spatial resolutions of the PA endoscopic probe. (a) Axial ESF measured by linearly translating the probe to images with the edge of a black tape. (b) Axial LSF calculated from the ESF shown in panel (a). (c) Tangential ESF measured by circularly scanning the edge of a black tape. (d) Tangential LSF calculated from the ESF shown in panel (c). (e) Time-resolved PA impulse response measured by the MRR ultrasonic sensor. (f) CNR calculated by the shift and sum method. Radial resolution was estimated at 6 dB (dashed line).

resolutions were quantified in ideal conditions, they should provide good estimations of the actual performances of the probe in tissue imaging when ultrasonic and optical scattering and attenuation present.

The performance of our PA endoscope also depends on the MRR's detection sensitivity stability during scanning. Circular scans can perturb the input PM fiber that may affect optical coupling by altering the intensity and polarization of the input laser, causing a shift in the MRR's resonance frequency. We examined the influence of the potential perturbation by performing a 360 deg circular scan and measuring the transmission spectra at every 10 deg increment. Figure 4(a) shows the detection sensitivities derived from the spectra at a fixed operating wavelength. Result shows a good consistency of detection sensitivities within a scan range of 180 deg, but sensitivity drops by as much as 30% when the angle is beyond 180 deg.

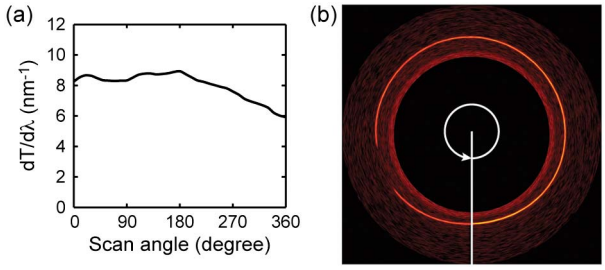

Fig. 4. (a) Angular sensitivity variation of the MRR-based PA endoscopic probe. (b) A full 360 deg B-scan of a cylindrical black tape strip.

To test PA imaging capability in a full 360 deg scan, a phantom sample was made by bending a strip of black tape to create an absorption surface with a cylindrical contour. Figure 4(b) shows a B-scan image of the phantom sample in polar coordinates, and the intensity variation is not visually obvious. The start and end positions of the scan (marked by the solid line in Fig. 4(b)) overlapped very well; however, their peak signals show a difference in intensity that agrees with the variation of angular sensitivity derived from the aforementioned sensitivity test. It suggests that the image from a circular scan needs to be compensated for by normalizing the corresponding angular sensitivity.

To demonstrate the volumetric imaging ability of the endoscopy PA system, we imaged two phantom samples (Fig. 5) that mimic actual anatomical features for endoscopic imaging. The first phantom was a hollow black plastic tube fabricated by 3D printing as shown in Fig. 5(a). The inner surface of the tube was intentionally designed to have an uneven wavy-pattern. Furthermore, the parallel ridge-like features were caused by the layer-by-layer extrusion deposition process of the 3D printing (Replicator 2, MakerBot), spaced at roughly 150 μm per layer. A cylindrical 90 deg scan inside the tube was performed and the reconstructed 3D rendering clearly resolved the morphology of its inner surface [Fig. 5(b)]. Figure 5(c) shows the A-line from the position highlighted in Fig. 5(b). Ridge-like features with a depth of less than 100 μm can be easily recovered in the axial cross-sectional view due to the improved spatial resolution. As noted, the PA signal strength from the valleys of the wavy surface tends to be weaker, caused by the high numerical aperture of the GRIN lens limiting the depth of focus.

The second phantom shown in Fig. 5(d) was used to test the system's ability to resolve fine features such as blood vessels in tissue. Strands of human hairs (diameters: ~100 μm) were randomly inserted and sandwiched between layers of semi-transparent tapes, which in turn were rolled into the shape of a tube. Figure 5(e) is the corresponding 3D PA image, showing clear boundaries between the highlighted hairs and the background. Figure 5(f) is the A-line from the position highlighted in Fig. 5(e), indicating a good SNR. To further illustrate the spatial orientation of each hair, a cross-section was taken and flattened to show the depth distribution of the imaged hairs. As a result of the high quality optical focus and higher radial resolution offered by MRR ultrasonic sensor, hair with a relevantly high absorption coefficient usually only appears at its top surface, showing a crescent-like shape in the cross-section view.

Although PA endoscopy offers optical absorption imaging with exceptional resolution at improved penetration depth, only limited endothelium tissues possess strong optical absorption contrasts. As a result, it is often difficult to locate fields of interest and to provide a comprehensive anatomic view, thus limiting the practicality of PA endoscopy. Recently, increasing attention has been directed to integrate PA endoscopy with other imaging modalities, such as optical confocal microscopy [22] and optical coherence tomography (OCT) [23,24]. Additional contrasts can serve as guides to direct endoscopic PAM toward a specific region of interest. Since the thin

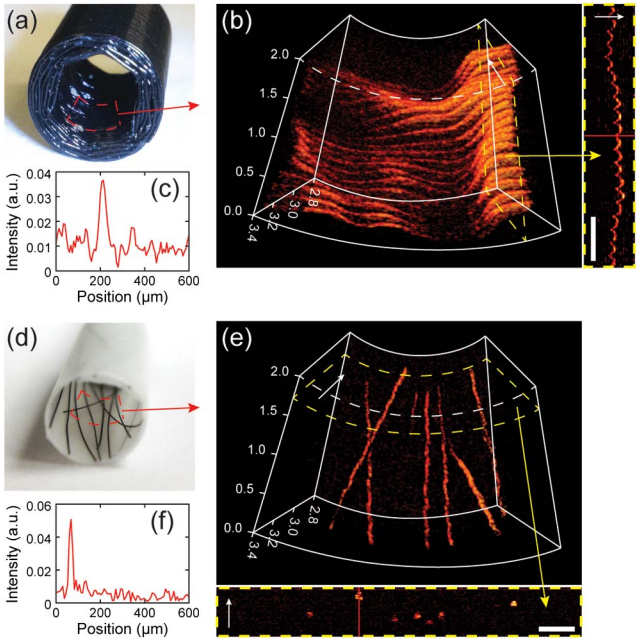

Fig. 5. Phantom imaging results. (a) Photograph of the black plastic tube phantom. (b) 3D PA volumetric rendering of its inner surface. Axial cross-section within the region marked by the dashed-box is shown in the right panel. Bar: 500 μm. (c) A-line signal from position marked by the red line in the right figure in panel (b). (d) Photograph of the hair phantom. (e) Volumatric rendering of the PA hair sample imaging. The flattened cross-sectional view within dashed-region is shown in the lower panel. Bar: 500 μm. (f) A-line signal from the position marked by the red line in the bottom figure in panel (e).

transparent MRR ultrasonic sensor was used in our design, multimodal incorporation can be easily achieved by inserting extra optical fibers to implement OCT or confocal microscopy without altering the optical design and ultrasound sensing components. Furthermore, the MRR ultrasonic sensor provides a sufficiently large detection bandwidth that significantly improves the radial resolution of PA endoscopy. Consequently, isometric voxels in volumetric imaging, for the first time, has been realized in PA endoscopy. This greatly benefits the spatial image registrations of PA imaging with other optical imaging modalities.

In summary, we developed a novel all-optical PA endoscopic probe and demonstrated the feasibility of using a polymeric MRR ultrasonic sensor for optical-resolution 3D PA endoscopic imaging. The all-optical design shows a potential method to realize a miniature PA probe without compromising its acoustic sensitivity. Adding PAM into multimodal endoscopes is highly desired in clinical applications and scientific research for offering complementary anatomical and functional contrasts in various diagnostic capacities (e.g., gastrointestinal pathologies, prostate cancer, and coronary artery disease). Our design offers the potential for a robust multimodal platform through the combination of endoscopic OCT and other optical imaging modalities.

We sincerely acknowledge the generous support from the National Institutes of Health grants 1R24EY022883 and 1R01EY019951 to HFZ, and the National Science Foundation grants CBET-1055379 and CBET-1066776 to HFZ, and CMMI-0955195 and CMMI-0751621 to CS.

References

1. L. V. Wang and S. Hu, Science **335**, 1458 (2012).
2. J.-M. Yang, C. Favazza, R. M. Chen, J. J. Yao, X. Cai, K. Maslov, Q. Zhou, K. K. Shung, and L. V. Wang, Nat. Med. **18**, 1297 (2012).
3. H. F. Zhang, K. Maslov, G. Stoica, and L. V. Wang, Nat. Biotechnol. **24**, 848 (2006).
4. T. Liu, Q. Wei, J. Wang, S. L. Jiao, and H. F. Zhang, Biomed. Opt. Express **2**, 1359 (2011).
5. M. R. Chatni, J. Xia, R. Sohn, K. Maslov, Z. Guo, Y. Zhang, K. Wang, Y. Xia, M. Anastasio, J. Arbeit, and L. V. Wang, J. Biomed. Opt. **17**, 0760121 (2012).
6. J. Yao, K. I. Maslov, and L. V. Wang, Technol. Cancer Res. Treat. **11**, 301 (2012).
7. J. A. Viator, G. Paltauf, S. L. Jacques, and S. A. Prahl, Proc. SPIE **4256**, 16 (2001).
8. S. Sethuraman, S. R. Aglyamov, J. H. Amirian, R. W. Smalling, and S. Y. Emelianov, IEEE Trans. Ultrason. Ferroelectr. Freq. Control **54**, 978 (2007).
9. J.-M. Yang, K. Maslov, H.-C. Yang, Q. Zhou, K. K. Shung, and L. V. Wang, Opt. Lett. **34**, 1591 (2009).
10. Y. Yuan, S. Yang, and D. Xing, Opt. Lett. **35**, 2266 (2010).
11. L. Xi, C. Duan, H. Xie, and H. Jiang, Appl. Opt. **52**, 1928 (2013).
12. Y. Yang, X. Li, T. H. Wang, P. D. Kumavor, A. Aguirre, K. K. Shung, Q. F. Zhou, M. Sanders, M. Brewer, and Q. Zhu, Biomed. Opt. Express **2**, 2551 (2011).
13. K. K. Shung, J. M. Cannata, and Q. F. Zhou, J. Electroceram. **19**, 141 (2007).
14. J. J. Niederhauser, M. Jaeger, M. Hejazi, H. Keppner, and M. Frenz, Opt. Commun. **253**, 401 (2005).
15. G. Brodie, Y. Q. Qiu, S. Cochran, G. Spalding, and M. Macdonald, IEEE Trans. Ultrason. Ferroelectr. Freq. Control **61**, 389 (2014).
16. G. Wild and S. Hinckley, IEEE Sens. J. **8**, 1184 (2008).
17. D. Gallego, M. Wang, J. Hiltunen, R. Myllyla, and H. Lamela, Proc. SPIE **8223** 822343 (2012).
18. E. Z. Zhang and P. C. Beard, Proc. SPIE **7899**, 78991F (2011).
19. H. Li, B. Dong, Z. Zhang, C. Sun, and H. F. Zhang, Sci. Rep. **4**, 4496 (2014).
20. J. Wang, T. Liu, S. Jiao, R. Chen, Q. Zhou, K. K. Shung, L. V. Wang, and H. F. Zhang, J. Biomed. Opt. **15**, 5 (2010).
21. G. Ku, K. Maslov, L. Li, and L. V. Wang, J. Biomed. Opt. **15**, 021302 (2010).
22. R. Kiesslich, J. Burg, M. Vieth, J. Gnaendiger, M. Enders, P. Delaney, A. Polglase, W. McLaren, D. Janell, S. Thomas, B. Nafe, P. R. Galle, and M. F. Neurath, Gastroenterology **127**, 706 (2004).
23. S. H. Yun, G. J. Tearney, B. J. Vakoc, M. Shishkov, W. Y. Oh, A. E. Desjardins, M. J. Suter, R. C. Chan, J. A. Evans, I.-K. Jang, N. S. Nishioka, J. F. de Boer, and B. E. Bouma, Nat. Med. **12**, 1429 (2006).
24. D. C. Adler, Y. Chen, R. Huber, J. Schmitt, J. Connolly, and J. G. Fujimoto, Nat. Photonics **1**, 709 (2007).